*Nucleic Acids Research*, 2025, **53**, gkaf222
https://doi.org/10.1093/nar/gkaf222
**Synthetic Biology and Bioengineering**

# Targeted translation inhibition of chloroplast and mitochondrial mRNAs by designer pentatricopeptide repeat proteins

**Nikolay Manavski [1,*], Serena Schwenkert [1], Hans-Henning Kunz [2], Dario Leister [1], Jörg Meurer [1]**

[1]Plant Molecular Biology, Faculty of Biology, Ludwig-Maximilians-Universität Munich, Großhaderner Street 2-4, 82152 Planegg-Martinsried, Germany
[2]Plant Biochemistry, Faculty of Biology, Ludwig-Maximilians-Universität Munich, Großhaderner Street 2-4, 82152 Planegg-Martinsried, Germany
[*]To whom correspondence should be addressed. Email: n.manavski@biologie.uni-muenchen.de

## Abstract

Pentatricopeptide repeat (PPR) proteins are crucial for organellar gene expression. To establish a tool for gene expression manipulation in Arabidopsis plastids and genetically inaccessible mitochondria, we engineered designer (dPPR) proteins to specifically inhibit the translation of organellar mRNAs by masking their start codons. Unlike prior methods for targeted downregulation of gene expression, which rely on re-targeting native PPR proteins to RNA sequences closely related to their original targets, our approach employs a synthetic P-type PPR scaffold that can be designed to bind any RNA sequence of interest. Here, using dPPR-*psbK* and dPPR-*nad7*, we targeted the *psbK* mRNA in chloroplasts and the *nad7* mRNA in mitochondria, respectively. dPPR-*psbK* effectively bound to *psbK* mRNA and inhibited its translation with high specificity, resulting in disrupted PSII supercomplexes and reduced photosynthetic efficiency. dPPR-*nad7* suppressed *nad7* translation, affecting NADH oxidase activity in complex I and growth retardation. Comparing phenotypes with tobacco *psbK* knockouts and *nad7* knockdown *bir6*-2 mutants, along with quantitative proteomics, showed no clear evidence of physiologically relevant off-target effects. Our findings establish dPPR proteins as precise tools for targeted translation inhibition, facilitating functional studies of organellar genes and offering a novel approach with potential for manipulating organellar gene expression in diverse plant species.

## Graphical abstract

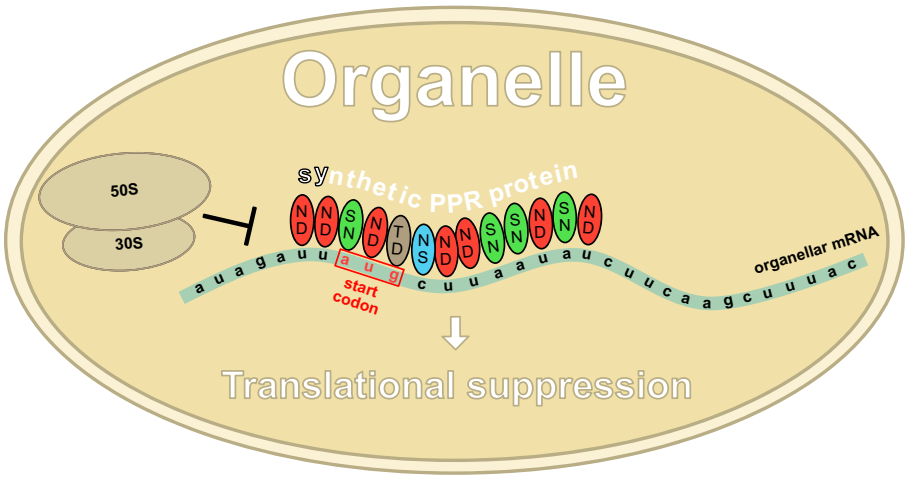


## Introduction

The genomes of plant plastids and mitochondria encode essential components for cellular processes. In Arabidopsis, the plastid genome comprises ∼110 genes, predominantly encoding proteins for the transcription–translation machinery and photosynthesis-related functions. This genetic framework is supplemented by ∼3000 nuclear-encoded proteins that support photosynthesis, plastid gene expression, and various

**Received:** October 19, 2024. **Revised:** March 3, 2025. **Editorial Decision:** March 4, 2025. **Accepted:** March 11, 2025

metabolic pathways localized in chloroplasts [1]. Similarly, the mitochondrial genome of Arabidopsis, containing ~60 genes, encodes critical components of the respiratory chain, ATP synthase complexes (I–V), and many proteins of unknown function. Additionally, it includes genes involved in protein translocation, cytochrome *c* biogenesis, ribosomal subunits, as well as transfer RNAs (tRNAs) and ribosomal RNAs (rRNAs) [2]. A significant number of these genes code for subunits of large protein complexes, but the mechanisms governing their biogenesis, assembly, and functionality remain largely elusive. To address and clarify these unresolved questions, various approaches have been established to allow genome manipulation in organelles. Transplastomic technologies have first been employed in tobacco plastids enabling detailed study of nearly all chloroplast protein-coding genes, with only a few exceptions such as *PsbK* and *Ycf5* [3].

Unlike chloroplasts, there are currently no feasible methods for transforming plant mitochondria. Consequently, indirect and in most cases laborious strategies have been developed to manipulate mitochondrial gene expression. For instance, transcription activator-like effector nucleases (TALENs) were used to knockout genes in rice, rapeseed, and tobacco [4–6]. Additionally, the DddA-derived cytosine base editor (DdCBE) promoted mutagenesis in mitochondria and chloroplasts [7]. Other approaches utilized tRNA-like ribozymes to decrease the expression of specific mitochondrial genes [8, 9]. Furthermore, the native PPR protein RPF2 was modified by altering the specificity of just two of its 16 PPR domains, enabling it to target and cleave segments of two new mRNA targets, *nad6* and *atp1*, which differ from the natural RPF2 target sequences located within the 5′-untranslated regions of *cox3* and *nad9* mRNAs at only two or three positions, respectively [10–12]. This targeted cleavage led to effective knockdown in the expression of *nad6* and *atp1*; however, this approach depends on and is restricted to sequence similarities between the RPF2's natural RNA targets and the newly targeted transcripts [13]. Here, we developed a different approach to alter organellar gene expression, employing synthetic customized pentatricopeptide repeat (PPR) proteins. Synthetic PPRs do not rely on sequence similarities to any naturally occurring RNA targets and can therefore be designed to bind virtually any RNA sequence of interest.

PPR proteins, prevalent in land plants, are RNA-binding proteins that regulate organellar gene expression at the post-transcriptional level. By binding to transcripts in a sequence-specific manner, PPR proteins influence various processes such as splicing, editing, processing, stability, and translation of their target RNAs. PPR proteins are defined by degenerate 35-amino acid repeat that form two antiparallel α-helices. When arranged in tandem arrays, these repeats create a super-helical structure that binds RNA in a one-repeat, one-nucleotide manner. The specificity of PPR protein binding is determined by two amino acids located at positions 5 and 35 within each repeat [14]. This understanding led to the development of the PPR recognition code, enabling the design of the first programmable synthetic PPR protein that was shown to bind specifically to its target RNA *in vitro* [15]. Applying this protein design, it has been previously demonstrated that synthetic PPR proteins are also functional *in vivo* [16, 17] and can substitute for endogenous PPR or other RNA-binding proteins [18, 19]. In this study, we employed a synthetic PPR scaffold to create a designer (d)PPR protein designated as dPPR-*psbK*. By modifying the two specificity-determining amino acids within each repeat, we designed dPPR-*psbK* to bind and mask the start codon of the *psbK* mRNA in the chloroplast. Furthermore, we designed a second dPPR protein, named dPPR-*nad7*, to target a segment located just downstream of the translation initiation codon of the mitochondrial *nad7* mRNA. Our findings demonstrate that binding of the dPPR proteins directly or adjacent to the start codon of the target mRNAs efficiently lower their translation rates. Studying the deleterious effects of downregulated *psbK* and *nad7* translation revealed a previously unknown role of PsbK in the formation of PSII supercomplexes in the chloroplast of vascular plants and confirmed the relevance of Nad7 for efficient NADH oxidase activity in mitochondria. Thus, targeted translation inhibition can now be added to the list of applications of dPPRs and represents a fast and efficient approach for the manipulation of gene expression in both organelles, chloroplast and mitochondria.

## Materials and methods

### Plant material and growth conditions

The *bir6-2* T-DNA line SALK_00 031 (At3g48250) was used [20]. All Arabidopsis plants were grown on soil under the following controlled conditions: 12-h light (20°C)/12-h dark (18°C) at a PFD of 100 μM photons $m^{-2}$ $s^{-1}$.

For immunodetection of mitochondrial proteins and RNA co-immunoprecipitation analysis, mitochondria were isolated from hydroponic seedling cultures. Seedling cultivation and mitochondria isolation were carried out as described previously [21].

*Nicotiana tabacum* and *Nicotiana benthamiana* plants were grown on soil under standard greenhouse conditions (16-h light/8-h dark cycle; 22°C; in average 200 μM photons $m^{-2}$ $s^{-1}$).

### Generation of transgenic lines

The coding sequences of dPPR-*psbK* and dPPR-*nad7* were codon-optimized for *Arabidopsis thaliana* (Supplementary Fig. S2), synthesized, and cloned into pDONR221 by Invitrogen. The delivered constructs, pDONR221:dPPR-*psbK* and pDONR221:dPPR-*nad7*, were then subcloned into pAUL1 [22] vector using LR II clonase (Invitrogen, Thermo Fisher Scientific) following the manufacturer's protocol. *Agrobacterium tumefaciens* GV3101 cells transfected with the resulting constructs, pAUL1:dPPR-psbK and pAUL1:dPPR-*nad7*, were used for floral dip transformation of Col-0 (WT) Arabidopsis plants. Transgenic plants of T1 generation were selected by Basta treatment and the expression of the transgenes was verified by immunodection with HA antibodies.

For generation of *psbK* knockouts in tobacco, a 3619 bp fragment, covering the tobacco chloroplast genome positions 6150 to 9769, and containing the *PsbK* gene was generated by BamHI restriction digest of clone B25 obtained from the tobacco plastome clone bank [23]. This fragment was inserted into the BamHI sites of the pBluescript II $KS^-$ (Stratagene Inc., La Jolla, CA). A terminatorless chimeric *aadA* cassette containing the tobacco 16S rRNA promoter was then cloned into the naturally occurring StuI site at position 85 of *PsbK* gene in reading frame orientation. This clone was used for transformation of tobacco leaves (*Nicotiana tabacum* cv Petit Havanna) via particle bombardment [3]. The transformed leaf pieces were selected, regenerated, and cultured on medium containing spectinomycin [24]. Three selected lines were then

backcrossed five times using WT pollen as donor and homoplastomy was confirmed by genotyping PCR.

## Immunoblot analyses and blue native–PAGE

Thylakoid membrane proteins, isolated as described in the RNA co-immunoprecipitation and slot blot hybridization section, were resuspended in thylakoid resuspension buffer [100 mM $Na_2CO_3$ and 10% (w/v) sucrose]. Proteins corresponding to 5 µg of chlorophyll were fractionated using SDS–PAGE on Tris-Tricine gels. For total protein extraction, 9-mm diameter leaf discs were homogenized in 100 µl of sample buffer (120 mM Tris–HCl, pH 6.8, 4% SDS, 20% glycerol, 2.5% β-mercaptoethanol, 0.01% bromophenol blue), and cell debris were pelleted by centrifugation (5 min at room temperature, 21 000 × *g*). Ten microliters of the supernatant were separated on SDS–PAGE using 12% Tris-glycine gels. Proteins were transferred onto polyvinylidene fluoride (PVDF) membranes by wet transfer using blotting buffer (25 mM Tris, 192 mM glycine, and 20% ethanol). Membranes were stained with Coomassie Brilliant Blue (CBB) G-250 solution [0.02% CBB G-250, 25% (v/v) methanol, and 10% (v/v) acetic acid] to control for efficient transfer and sample loading. Destained membranes were blocked for 1 h at room temperature using TBST buffer [25 mM Tris–HCl, pH 8, 150 mM NaCl, and 0.1% (v/v) Tween 20] supplemented with 5% (w/v) skim milk powder and incubated overnight at 4°C in the blocking buffer containing primary antibodies. Membranes were then washed three times with TBST buffer and incubated with secondary antibodies in TBST supplemented with 2.5% (w/v) skim milk powder. After an additional three washes with TBST, signals were detected using SuperSignal West Pico Plus Chemilumescent Substrat (Pierce, Thermo Fisher Scientific) and read with a Fusion FX7 system (PeqLab).

Antibodies against PsbI (AS06-158, 1:5000), PsbA (AS05-084, 1:10 000), PsbD (AS06-146, 1:5000), PsaA (AS0-6172, 1:5000), PsaB (AS10-695, 1:1000), PetB (AS18-4169, 1:5000), Lhcb2 (AS01-003, 1:5000), AOX1/2 (AS04-054, 1:1000), Cox2 (AS04-053A, 1:1000), and AtpB (AS05-085, 1:5000) were obtained from Agrisera. PsbK (PHY4392A, 1:1000) and Nad7 (PHY1077S, 1:1000) were acquired from PhytoAB; monoclonal HA antibodies (H9658, 1:5000) were purchased from Sigma–Aldrich and GFP antibodies (50430-2-AP, 1:2500) from Proteintech. AtpF (1:1000), NdhH (1:1000), Nad9 (1:10 000), and CS (1:10 000) were kindly provided by Richard J. Berzborn (University of Bochum), Klaus Steinmüller (University of Düsseldorf), Hans-Peter Braun (University of Hannover), and Iris Finkemeier (University of Münster), respectively. The following secondary antibodies were used: Goat Anti-Rabbit, IgG Antibody, HRP-conjugate (Sigma–Aldrich, A9169, 1:25 000), and Goat Anti-Mouse IgG (Jackson Immuno Reasearch, 115-035-062, 1:10 000).

Thylakoid membranes for blue native (BN)–PAGE were isolated and solubilized as described previously [25]. Photosynthetic complexes were separated in the first dimension using precast NativePAGE™ 3%–12%, Bis-Tris, 1.0 mm, and mini protein gels (Invitrogen), according to the manufacturer's instructions. Lanes were denatured for 30 min in denaturation buffer (2% SDS, 66.7 mM $Na_2CO_3$, and 100 mM Dithiothreitol (DTT)) and separated in the second dimension using SDS–PAGE on 12% Tris-Tricine gels. Gels were then stained with Roti-Blue quick solution (Carl Roth).

BN–PAGE of mitochondrial respiratory complexes and subsequent complex I activity staining were performed as described previously [26]. Ten-day-old seedlings from hydroponic cultures were used.

## Photosynthetic measurements

A pulse amplitude-modulated system (Dual-PAM 100, Walz Photosynthetic Instruments) was used to measure the PSII maximum quantum yield (*Fv*/*Fm*), the effective PSII quantum yield [Φ(PSII)], nonregulated nonphotochemical quenching yield [Φ(NO)], the quantum yield of PSI [Φ(PSI)], as well as acceptor [Φ(NA)], and donor side [Φ(ND)] limitation at PSI. Actinic light intensities of 80 µmol photons $m^{-2}$ $s^{-1}$ and saturating light pulses with a duration of 800 ms and a light intensity of 6000 µmol photons $m^{-2}$ $s^{-1}$ were used. Fluorescence parameters were taken in the steady state 5 min after induction. Chlorophyll fluorescence imaging was performed using the Hexagon-Imaging-PAM (Walz Photosynthetic Instruments).

Thermoluminescence (TL) measurements were conducted to assess the impact of PsbK loss on electron transport within PSII. Leaf discs (10 mm) were dark-adapted for 30 min at 20°C, rapidly cooled to −1°C with liquid nitrogen, and then illuminated with a single-turnover flash to induce charge separation in PSII centers. The samples were warmed to 60°C at a rate of 1°C/s, and the B-band light emission was measured during the heating, which primarily reflects the recombination of the S2/S3QB-charge pair and typically appears around 30°C in plants [27].

## Protein purification and EMSA

The coding sequences of dPPR-*psbK* and dPPR-*nad7*, excluding the transit peptides, were PCR amplified using primers Fw dPPR-*psbK*/-*nad7* BamHI and Rev dPPR-*psbK*/-*nad7* BclI (primer details are provided in Supplementary Table S1). The PCR products were digested with BamHI/BclI and cloned into the BamHI/SalI restriction sites of the pMAL-Tev vector (generously provided by Alice Barkan, University of Oregon). The resulting constructs were transformed into Rosetta 2 (DE3) cells (Merck). Cultures were grown to an $OD_{600}$ of 0.5, and recombinant protein expression was induced with 1 mM isopropyl β-D-1-thiogalactopyranoside (IPTG). Cells were grown for 3 h at 20°C with shaking (200 rpm), then harvested by centrifugation (15 min at 4°C, 5000 × *g*) and lysed in lysis buffer [30 mM Tris–HCl, pH 7.5, 450 mM NaCl, 5 mM β-mercaptoethanol, and cOmplete™ EDTA-free Protease Inhibitor Cocktail (Roche)] via sonication. The lysates were cleared by centrifugation (15 min at 4°C, 21 000 × *g*) and incubated with amylose resin (NEB) for 1 h at 4°C with rotation (10 rpm). The resin was washed three times with lysis buffer, and proteins were eluted in the same buffer supplemented with 150 mM maltose.

Proteins were further purified using the Äkta pure system with a Superdex® 200 Increase 10/300 GL column and running buffer (100 mM Tris–HCl, pH 7.5, 150 mM NaCl, 1 mM EDTA, and 5 mM β-mercaptoethanol). Fractions containing the purified proteins were concentrated, supplemented with 50% glycerol, and stored at −80°C until use.

Electrophoretic mobility shift assays (EMSAs) were performed as described previously [18], with the modification that gels were not dried but frozen at −80°C while exposed to phosphor imaging screens.

## Subcellular localization analyses

For subcellular localization studies, pDONR221:dPPR-*psbK* and pDONR221:dPPR-*nad7* were cloned into pB7FWG2 using LR clonase II (Invitrogen, Thermo Fisher Scientific). Tobacco leaf infiltration and protoplast isolation was carried out as described previously [18]. The Axio Imager fluorescence microscope (Zeiss) was used to detect chlorophyll autofluorescence, eGFP signals, and to capture bright-field images of protoplasts.

## Polysome loading analysis

Polysome analysis of chloroplast transcripts was performed using 2-week-old plants, while polysome loading of mitochondrial mRNAs was examined in 10-day-old seedlings grown in hydroponic culture (see above). Experiments were conducted as previously described [28]. Recovered RNA was resuspended in gel loading buffer [6% (v/v) formaldehyde, 42% (v/v) deionized formamide, 1× 3-(N-Morpholino)propanesulfonic acid (MOPS) buffer, pH 8.0, 0.01% (v/v) bromophenol blue, and 0.01% (v/v) xylencyanol] and denatured for 5 min at 70°C. RNA was then separated on 1.2% agarose gels prepared with 1× MOPS buffer (pH 8.0) and 6% (v/v) formaldehyde, using a running buffer containing 1× MOPS buffer (pH 7.0) and 3.7% (v/v) formaldehyde. RNA was transferred onto Hybond-N + membrane (GE Healthcare) overnight by capillary transfer using 20× SSC buffer and immobilized by UV crosslinking.

For the detection of chloroplast transcripts, 80-mer DNA oligos were 5′-end radiolabeled using T4 polynucleotide kinase (NEB), according to the manufacturer's instructions. Mitochondrial mRNAs were detected using radiolabeled *in vitro* transcripts complementary to the target mRNAs. These transcripts were generated using T7 RNA polymerase with PCR templates containing a T7 promoter and [α32P] UTP, following the manufacturer's protocol (Thermo Fisher Scientific).

Blots were hybridized overnight either at 55°C (for DNA oligos) or at 68°C (for *in vitro* transcripts) in PerfectHyb™ Plus hybridization buffer (Merck). The blots were then washed twice in washing buffer (1× SSC and 0.1% SDS) and exposed to phosphor imaging screens.

## RNA co-immunoprecipitation and slot blot hybridization

Chloroplasts were prepared from 2-week-old WT and dPPR-*psbK* plants. Leaves were homogenized in extraction buffer [0.45 M Sorbit, 20 mM Tricine, pH 8.4, 10 mM EDTA, 10 mM $NaHCO_3$, and 0.1% (w/v) BSA] using a Waring blender. The homogenate was filtered through two layers of Miracloth and then centrifuged at 1500 × *g* for 7 min at 4°C. Chloroplasts were washed in washing buffer (0.3 M Sorbit, 20 mM Tricine pH 8.4 KOH, 2.5 mM EDTA, and 5 mM $MgCl_2$), resuspended in lysis buffer (30 mM HEPES pH 7.7, 10 mM MgAct, 60 mM KAct, 1 mM DTT, supplemented with Protease Inhibitor Cocktail [Roche]) and incubated for 30 min on ice with occasional vortexing. Lysates were cleared by centrifugation (4°C, 15 min, 21 000 × *g*). Pellets containing thylakoids were used for immunoblot analyses (see "Immunoblot analyses and BN–PAGE" section), while supernatants containing stroma proteins were used for RIP analysis. Five hundred micrograms of stromal extract was mixed with an equal volume of co-immunoprecipitation buffer [20 mM Tris (pH 7.5), 150 mM NaCl, 1 mM EDTA, 0.5% (v/v) Nonidet P40, and Protease Inhibitor Cocktail (Roche)] and incubated with 2 µl of anti-HA antibodies for 1 h at 4°C with rotation at 10 rpm. After adding 100 µl of Protein A Magnetic Beads (NEB), samples were incubated for another hour at 4°C with rotation at 10 rpm. Following five washes with co-immunoprecipitation buffer, the beads were resuspended in 100 µl of co-immunoprecipitation buffer (without protease inhibitors), supplemented with 0.1% (v/v) SDS and Proteinase K (0.1 µg/µl), and incubated for 30 min at 37°C. RNA was then purified by phenol–chloroform extraction and ethanol precipitation.

Mitochondria isolated from dPPR-*nad7* plants were lysed in lysis buffer [10 mM HEPES-KOH, pH 7.7, 100 mM KCl, 5 mM $MgCl_2$, 0.5% (v/v) Triton X-100, and 2 mM DTT, supplemented with Protease Inhibitor Cocktail (Roche)] for 30 min on ice with occasional vortexing. Lysates were cleared by centrifugation (4°C, 15 min, 21 000 × *g*) and diluted with an equal volume of co-immunoprecipitation buffer [20 mM Tris (pH 7.5), 150 mM NaCl, 1 mM EDTA, 5 mM $MgCl_2$, 0.5% (v/v) Nonidet P40, and Protease Inhibitor Cocktail (Roche)]. Five hundred micrograms of aliquots were incubated with either 2 µl of anti-HA antibodies or control IgGs (not recognizing Arabidopsis mitochondrial proteins) for 1 h at 4°C with rotation at 10 rpm. Antibody capture and RNA purification followed the same method as described above.

For slot blot analysis, the recovered RNAs were resuspended in 2× SSPE buffer (20 mM $NaH_2PO_4$, 300 mM NaCl, and 2 mM EDTA, pH 7.4), denatured for 10 min at 70°C, and blotted onto a Hybond-N + membrane (GE Healthcare) using a slot-blot device (Bio-Rad). RNA was immobilized by UV crosslinking. Probe generation and RNA hybridization were carried out as described in the polysome loading analysis.

## Quantitative proteomics

Protein extraction and preparation for proteomics samples followed previously established methods [29]. Briefly, frozen rosette leaf tissue was ground, and 50 mg of the resulting powder was resuspended in extraction buffer containing 100 mM HEPES (pH 7.5), 150 mM NaCl, 10 mM DTT, 6 M guanidine Chloride, and Roche cOmplete™ Protease Inhibitor Cocktail. Samples were sonicated using a Branson Sonifier B-12 (Branson Ultrasonics, Danbury, USA) followed by incubation at 60°C for 10 min. After centrifugation at 10 000 × *g* for 15 min, proteins were precipitated using a chloroform–methanol method. The protein precipitate was collected and washed with methanol, dried and resuspended in 3 M Urea, 2 M thiourea, and 50 mM HEPES (pH 7.8). Protein concentration was quantified using the Pierce 660 nm Protein Assay Kit (Pierce, Thermo Fisher Scientific). For downstream processing, 100 µg of protein was reduced with 10 mM DTT at 37°C for 30 min, followed by alkylation with 50 mM iodoacetamide (IAA) in darkness at room temperature for 20 min. Proteins were then digested overnight at 37°C with 1 µg of Trypsin (Pierce, Thermo Fisher Scientific). The resulting peptides were purified using homemade C18 stage tips [30], and 200 ng of purified peptides was used for LC-MS/MS analysis. Four biological replicates per genotype were analyzed.

Liquid chromatography–tandem mass spectrometry (LC-MS/MS) was performed on a nano-LC system (nanoElute2, Bruker Daltonics) coupled to a timsTOF HT mass spectrometer (Bruker Daltonics) using a CaptiveSpray nano electrospray ionization (ESI) source. The nano-LC system was equipped

with an PepMap Neo 5 μM trap column (C18, 300 μm × 5 mm, Thermo Fisher Scientific) and a PepSep Ultra separation column (C18, 25 cm × 75 μm × 1.5 μm, Bruker Daltonics). The peptide mixture was separated over a 60-min linear gradient of 5%–37% (v/v) acetonitrile at a constant flow rate of 250 nl $min^{-1}$. The column was kept at 50°C in a column oven throughout the run. Data independent acquisition (DIA) was performed using the method DIA PASEF-short gradient with the following settings: mass range: 100–1700 *m/z*, ion mobility range: 0.85–1.3 $Vs/cm^2$, ramp time: 100 ms.

Raw files were processed using DIA-NN v1.9.1 [31]. A library free search was performed against the Arabidopsis reference proteome including contaminants (Uniprot, www.uniprot.org, version April 2024) with default settings and match-between runs enabled. The DIA-NN output was processed with DIAgui [32]. Contaminates were removed, proteins and protein groups were filtered at a *Q*-value of 0.01 and $log_2$ label-free quantification (LFQ) using the MaxLFQ algorithm [33] was performed. Downstream statistical analysis was performed using Perseus version 2.0.11 [34], and graphs were prepared with R and RStudio v4.4.1 [35, 36]. All biological replicates were grouped and $log_2$ LFQ intensities were filtered to contain valid values in at least three of the four replicates in at least one group. To enable statistical evaluation, missing values were imputed with random numbers drawn from a normal distribution. Enrichment analysis was performed with ShinyGO 0.82 (Ge and Yao 2020).

The mass spectrometry proteomics data have been deposited to the ProteomeXchange Consortium via the PRIDE partner repository with the dataset identifier PXD060146. Proteins identified by mass spectrometry and statistical analysis can be found in Supplementary Table S2.

## Results

### dPPR-*psbK*

The start codon signals the initiation of protein synthesis, serving as the site where ribosomes begin translating mRNAs into proteins. To inhibit translation initiation in a specific, targeted manner, a designer pentatricopeptide repeat (dPPR) protein was engineered to bind to and mask the start codon of the chloroplast *psbK* mRNA, following the design of synthetic PPR proteins described previously [18]. In short, the dPPR protein, named here dPPR-*psbK*, consists of 13 consecutively arranged consensus PPR domains that are flanked by the N- and C-terminal domains of the PPR10 protein from maize (Supplementary Figs S1 and S2). According to the PPR code, the amino acids at positions 5 and 35 within each PPR repeat were modified to program the dPPR-*psbK* protein to recognize a 13-nucleotide region of the *psbK* mRNA including the start codon (position −2 to +11, relatively to the AUG). The dPPR-*psbK* construct was further equipped with the N-terminal transit peptide of RecA, enabling the protein to target chloroplasts, and a C-terminal HA tag for biochemical analyses.

First, the ability of dPPR-*psbK* to recognize its intended target was validated *in vitro*. Increasing concentration of *E. coli*-purified dPPR-*psbK*, lacking the RecA transit peptide, was used in an EMSA utilizing the target RNA sequence of *psbK* or a control RNA of an unrelated sequence. The dPPR-*psbK* protein bound to the *psbK* RNA with high affinity but, as expected, failed to bind to the control RNA (Fig. 1A), indicating that dPPR-*psbK* is indeed capable of specifically recognizing its destined target RNA sequence. Next, the subcellular localization of dPPR-*psbK* was examined. To this end, a dPPR-*psbK*-eGFP construct was transiently expressed in *N. benthamiana* leaves and the localization of dPPR-*psbK*-GFP to the chloroplast was confirmed by fluorescence microscopy of isolated protoplasts (Fig. 1B).

Given the specific *in vitro* RNA binding and correct subcellular localization, transgenic lines expressing dPPR-*psbK* under the control of the strong cauliflower mosaic virus 35S promoter were then generated in *A. thaliana* Col-0 (wild-type, WT) background. Three independent Basta-resistant primary transformants (T1 generation), dPPR-*psbK* #1–3, showing retarded plant growth and a pale green phenotype were selected for further phenotypic and molecular analyses (Fig. 1C). The expression of the transgene in dPPR-*psbK* #1–3 lines was confirmed by immunodetection and it remained stable over four generation (T4) (Supplementary Fig. S3).

In addition, three photoautotrophic *psbK* knockout mutants were generated in *N. tabacum* using a transplastomic approach, and homoplastomy was confirmed by genotyping PCR and immunodetection (Supplementary Fig. S4). Transgenic dPPR-*psbK* lines in Arabidopsis were then compared with Δ*psbK* tobacco mutants. All transformants showed significantly reduced and comparable *Fv*/*Fm* values, indicating primary defects in photosystem II (PSII) (Fig. 2A and B). This was concomitant with a reduced Φ(PSII) and an increased Φ(NO), reflecting decreased photosynthetic efficiency and elevated oxidative stress, respectively. Increased Φ(NO) values are associated with unregulated, nonphotochemical energy dissipation in closed PSII reaction centers, indicating a plant's inability to protect itself from light-induced damage and its susceptibility to PSII photoinactivation [37]. Additionally, there was a concurrent reduction in Φ(PSI) and severe donor-side limitation due to restricted PSII activity, while acceptor-side limitation remained unaffected in all transformants (Fig. 2B). Importantly, both Arabidopsis and tobacco Δ*psbK* mutants behaved almost identically in all respects, indicating that the phenotype observed in dPPR-*psbK* lines was due to the specific targeting of *psbK*, making relevant off-target effects unlikely.

PsbK has been reported to pay a role in the formation of the PSII reaction center complex and to be essential for photoautotrophic growth in *Chlamydomonas* [38]. In contrast, *psbK* mutants in *Synechocystis* sp. PCC 6803 and *Thermosynechococcus elongatus* BP-1 did not exhibit impaired phototrophic growth or oxygen-evolving activity of PSII [39, 40]. The role of PsbK as a photosystem II subunit in vascular plants has not been elucidated yet. To gain insights into the function of PsbK and to assess whether the similar phenotypes observed in Arabidopsis dPPR-*psbK* and tobacco Δ*psbK* share the same molecular basis, BN–PAGEs of photosynthetic thylakoid complexes were conducted. In the first BN dimension, a distinct reduction in the levels of PSII supercomplexes—composed of PSII core dimers associated with a variable number of light-harvesting complex II (LHCII) trimers—was evident (Fig. 3A and B). Resolution of photosynthetic complexes in the second dimension confirmed impaired formation of PSII supercomplexes and revealed a concomitant accumulation of free LHCII trimers/assembly complexes. These findings suggest that PsbK is required for the formation of PSII supercomplexes and seems to facilitated the attach-

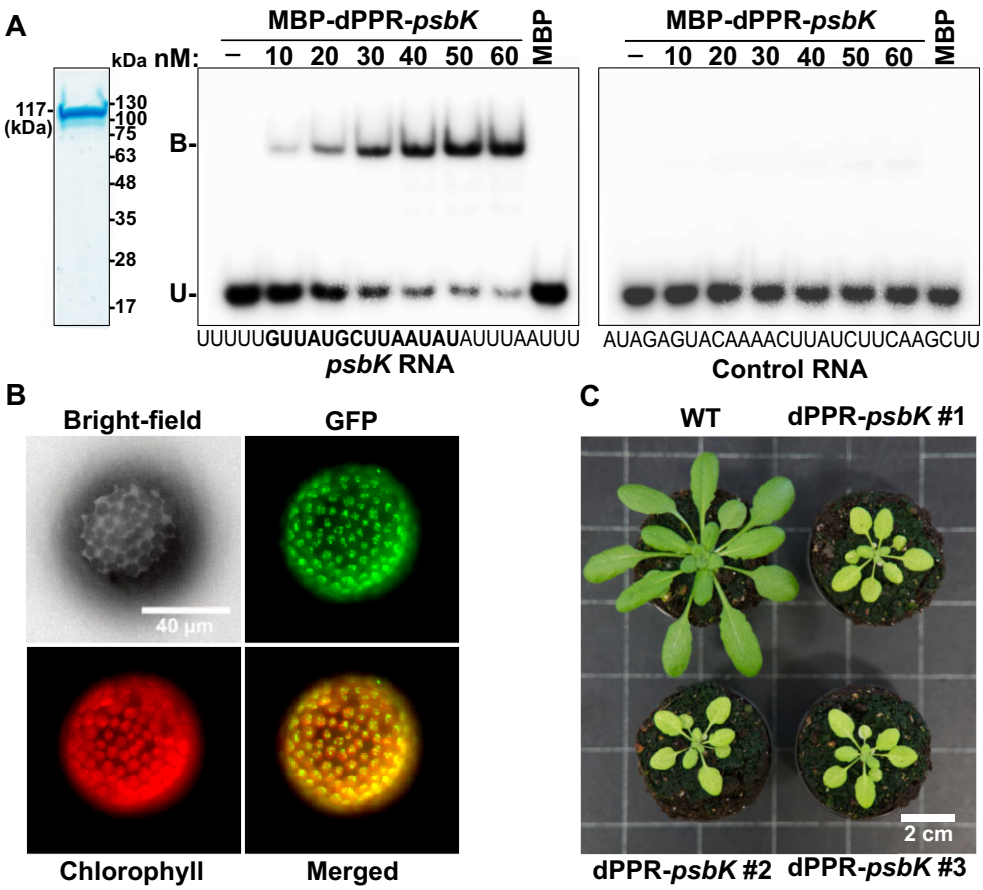


**Figure 1.** *In vitro* binding, subcellular localization, and phenotype of dPPR-*psbK* mutant plants. (**A**) EMSA with increasing concentrations of purified dPPR-*psbK* fused to maltose-binding protein (MBP) and radiolabeled RNA containing the target *psbK*-binding site (highlighted in bold). A control EMSA with RNA of unrelated sequence demonstrates binding specificity. Reactions using purified MBP protein show that MBP alone does not bind RNA. The purity of MBP-dPPR-*psbK* was confirmed by SDS–PAGE followed by CBB staining. B represents bound, and U represents unbound RNA. (**B**) Chloroplast localization of transiently expressed dPPR-*psbK*-GFP in isolated *N. benthamiana* protoplasts. Images show eGFP fluorescence, chlorophyll autofluorescence, a merged image of both signals, and a bright-field image of the protoplast. (**C**) Phenotypic comparison of three independent dPPR-*psbK* transgenic lines grown alongside WT plants, shown at 3 weeks of age.

ment of PSII antenna to the PSII core complexes, which appear capable of forming even in the absence of PsbK. TL measurements further support this, showing that the B bands were not shifted in dPPR-*psbK* and Δ*psbK* lines, indicating that PSII energetics and electron transfer are largely unaffected by the mutations, and PsbK is likely involved in antenna attachment or exciton transfer, rather than the core reaction center functionality (Supplementary Fig. S4).

Next, we confirmed the specific *in vivo* association of dPPR-*psbK* with *psbK* mRNA by RNA co-immunoprecipitation coupled with slot blot hybridization (RIP-slot blot). As expected, *psbK* was the most enriched RNA among all tested transcripts (Supplementary Fig. S5). To determine whether the binding of dPPR-*psbK* to the *psbK* start codon region effectively inhibits its translation, we examined PsbK steady-state levels of. In the three mutant lines expressing dPPR-*psbK*, PsbK proteins were undetectable in total protein extracts using PsbK-specific antibodies, with only trace amounts observed in isolated thylakoids (Fig. 4A). Other photosynthetic subunits of thylakoid membrane complexes accumulated to normal WT levels, indicating a specific translation inhibition of the *psbK* message (Fig. 4A). A more direct evidence for the specific translation inhibition of *psbK* was provided by polysome loading analysis. Generally, mRNAs with lower translation rates are less associated with polysomes, making them lighter and preventing them from migrating deeper into the sucrose gradient. Consequently, such mRNAs are found in the lighter fractions. *PsbK* is co-transcribed with *psbI* and *trnS* as tricistron and it is post-transcriptionally processed into two other isoforms: the dicistron *psbK-psbI* and the monocistron *psbK*. If *psbK* translation is successfully inhibited, all three RNA isoforms should exhibit reduced polysome loading. Indeed, *psbK* transcripts in the WT migrated far deeper into the gradient as compared to the *psbK* transcripts from the dPPR-*psbK* mutant (Fig. 4B). Notably, the monocistronic isoform of *psbK* in the WT reached the bottom of the gradient with peak signals in fractions 6 and 7, while in the dPPR-*psbK* mutant, monocistronic *psbK* remained only in the first three fractions. Translation initiation on the *psbI* message appears to occur independent of that of *psbK*, as *psbI* containing isoforms are loaded with polysomes, consistent with the unaffected PsbI protein accumulation in dPPR-*psbK* lines (Fig. 4A). Polysome loading of the control transcripts *psbA* and *psaA* was comparable to the WT, demonstrating that the observed translation impairment is specific and restricted to the *psbK* mRNA.

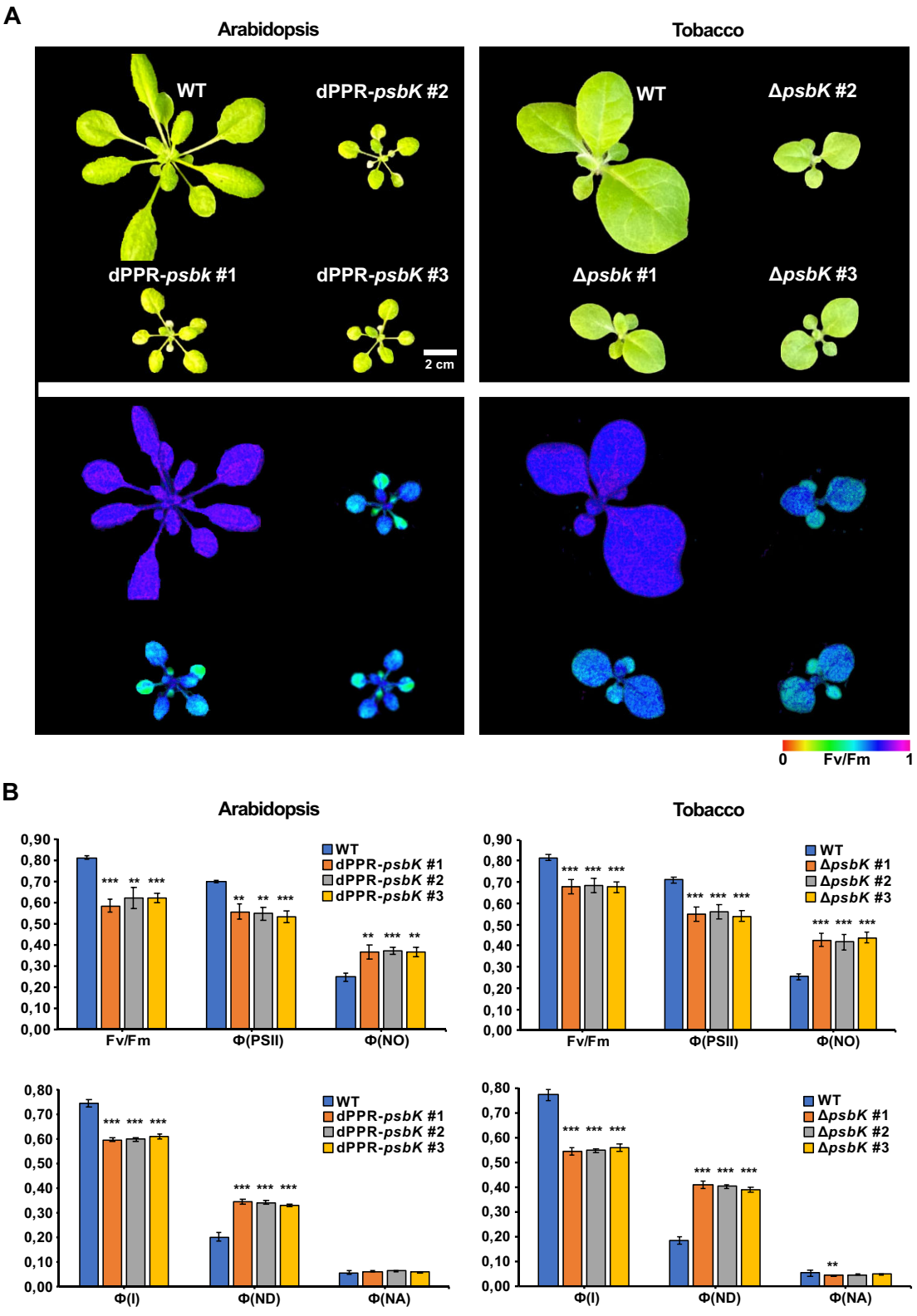


**Figure 2.** Phenotype comparison and photosynthetic performance of Arabidopsis dPPR-*psbK* lines and tobacco *psbK* knockout plants. (**A**) Images of 3-week-old Arabidopsis and tobacco plants with corresponding chlorophyll fluorescence imaging (*Fv*/*Fm*) below. Plant genotypes are labelled. Effective quantum yields of PSII are displayed on a false-color scale. (**B**) Photosynthetic parameters *Fv*/*Fm*, Φ(II), Φ(NO), Φ(**I**), Φ(ND), and Φ(NA) calculated for the plants shown in (A). Statistically significant differences from the WT are determined using Student's *t*-tests (**$P \leq 0.01$, ***$P \leq 0.001$).

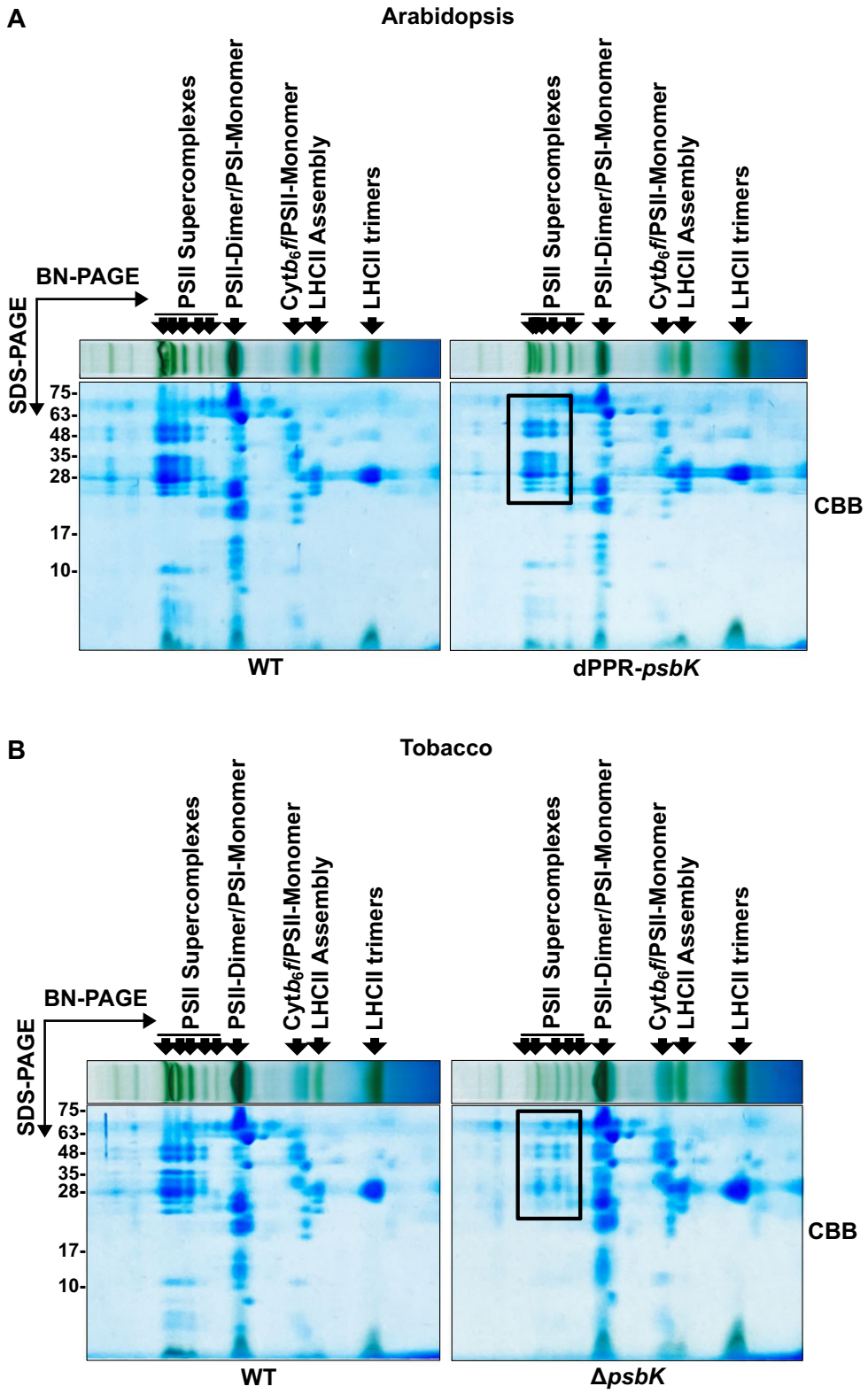


**Figure 3.** Molecular phenotype of Arabidopsis and tobacco *psbK* mutants examined by BN–PAGE. Chlorophyll-normalized, solubilized thylakoid complexes from Arabidopsis (**A**) and tobacco plants (**B**) were separated by BN–PAGE followed by SDS–PAGE and CBB staining of the second dimension. Protein complexes in the first dimension are indicated, genotypes are labeled. The squares highlight the reduced levels of PSII supercomplexes in both dPPR-*psbK* and Δ*psbK* mutants. Sizes of the protein marker bands (kDa) are indicated on the left side of the gels.

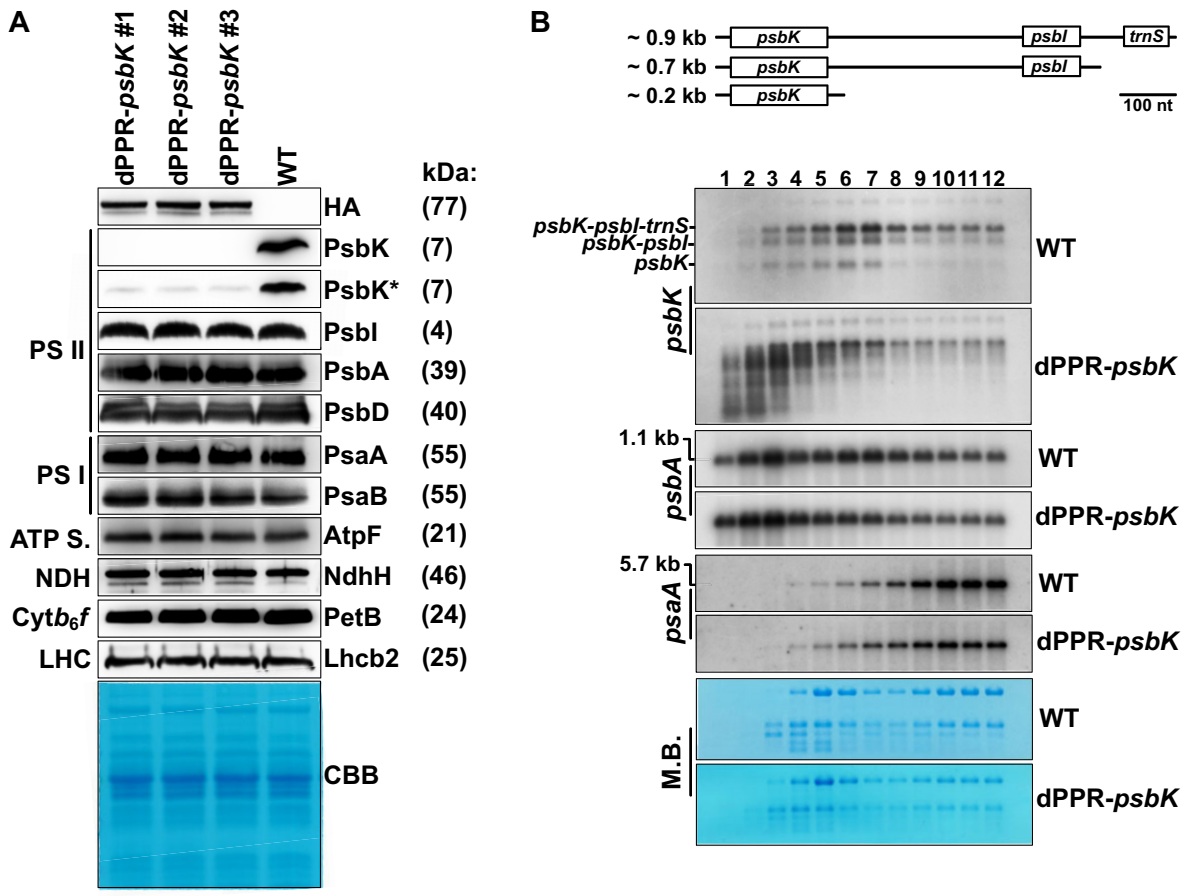


**Figure 4.** Suppression of *psbK* translation in dPPR-*psbK* plants. (**A**) Steady-state levels of representative subunits of photosynthetic complexes. Immunoblot analyses were conducted using isolated thylakoids normalized to equal chlorophyll levels. For immnodecoration of the soluble dPPR-*psbK* protein, total protein extracts normalized to fresh weight were used. PsbK was detected in total protein and thylakoids (*). CBB staining was used as loading control. The detected proteins and their corresponding molecular weights are shown on the right, while the associated thylakoid membrane complexes are indicated on the left. ATP S., ATP synthase. (**B**) Polysome loading analysis of *psbK* and control transcripts *psbA* and *psaA* in WT and dPPR-*psbK* plants. Methylene Blue (M.B.) staining of the recovered fractions [1–12] is shown. The three different *psbK* transcript isoforms (mono-, di-, and tricistron) are indicated and illustrated schematically above the blots.

## dPPR-*nad7*

To underscore the general application of dPPRs as a reliable tool for targeted inhibition of organellar translation, we targeted another transcript to provide an independent example. Given the lack of feasible methods for manipulating mitochondrial gene expression to date, we chose to inhibit the translation of *nad7* mRNA in mitochondria. If successful, this would represent a highly valuable, rapid, and effective approach for manipulating mitochondrial gene expression. Following the design described for dPPR-*psbK*, we reprogrammed the dPPR protein to recognize a 13-nucleotides segment within the coding sequence of *nad7* in the region +4 to +16 adjacent to the start codon (Supplementary Fig. S1). Additionally, we introduced the mitochondrial targeting signal of the ATPase β3 subunit to direct dPPR-*nad7* to the mitochondria. We chose not to mask the start codon with dPPR-*nad7* binding to avoid losing mutants if complete inhibition of *nad7* translation results in a lethal phenotype.

Experiments analogous to those performed with dPPR-*psbK* were conducted with dPPR-*nad7*. In brief, *in vitro* binding studies and subcellular localization analysis confirmed specificity of binding (Fig. 5A) and the mitochondrial localization of dPPR-*nad7* (Fig. 5C). Following the transformation of WT plants, three independent dPPR-*nad7* transgenic lines (#1–3) expressing the dPPR-*nad7* at different levels and showing varying degrees of growth retardation were selected (Fig. 5B and D). The levels of dPPR-*nad7* expression correlated with the extend of *nad7* translation suppression and with the degree of growth impairment (Fig. 5B and D). The phenotypes of the dPPR-*nad7* lines were compared with the WT and with the *nad7* knockdown mutant *bir6-2*. *Bir6-2* is a T-DNA insertion line disrupted in the At3g48250 locus, which encodes a PPR protein required for the efficient splicing of intron 1 of the mitochondrial *nad7* transcript [20]. Among the three mutant lines, dPPR-*nad7* #1 expressed the transgene at the highest levels and most efficiently suppressed *nad7* translation. dPPR-*nad7* #1 most closely resembled the phenotype of *bir6-2* and was therefore chosen for further analysis.

Similar to dPPR-*psbK*, *in vivo* association of dPPR-*nad7* with the *nad7* mRNA was validated by RIP-slot blot analysis (Supplementary Fig. S6). Next, we examined the steady-state levels of various subunits of mitochondrial complexes in total mitochondrial extracts obtained from WT, *bir6-2*, and dPPR-*nad7* seedlings. As mentioned above, the expression of

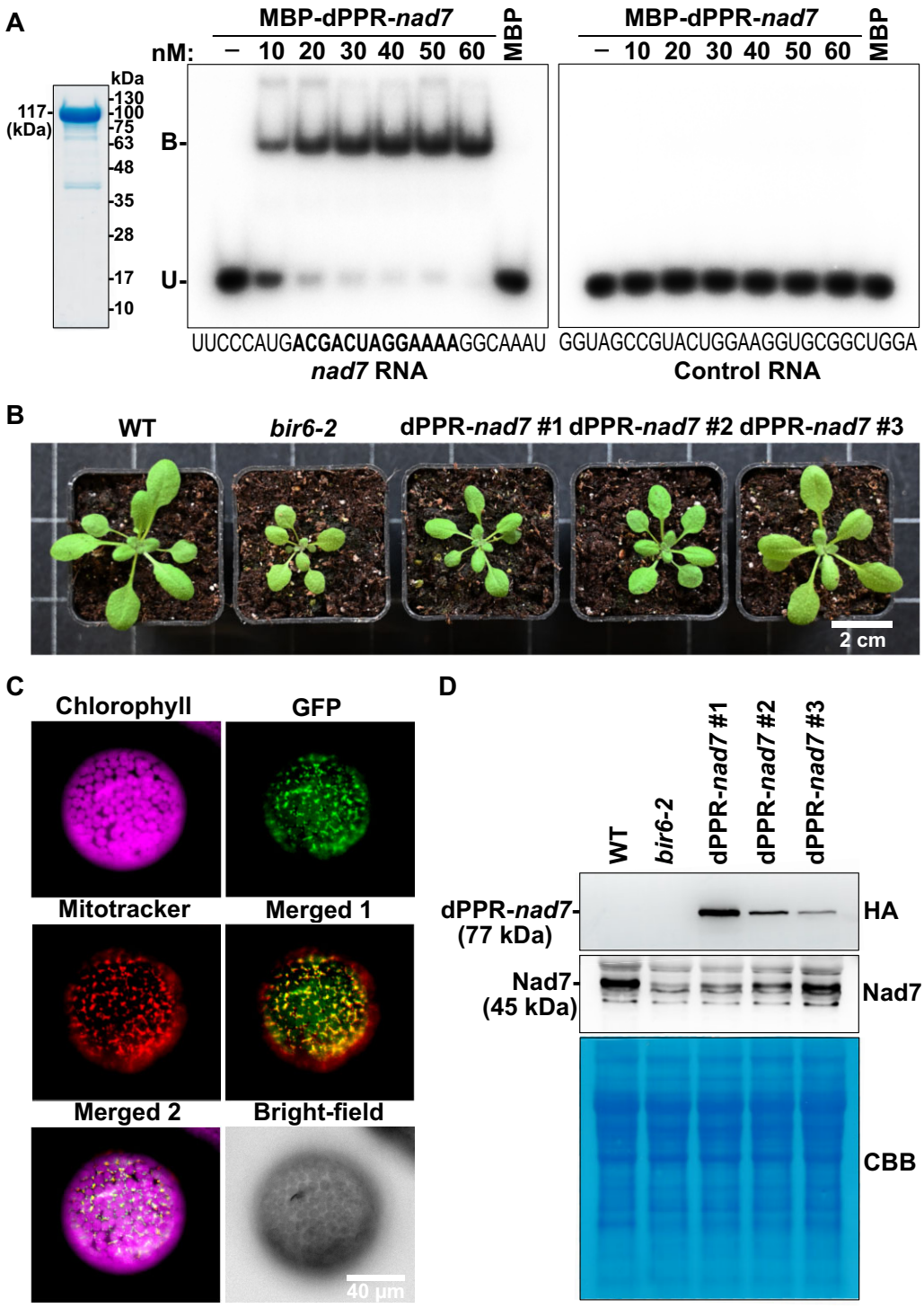


**Figure 5.** *In vitro* RNA recognition, phenotype, and subcellular localization of dPPR-*nad7*. (**A**) EMSA conducted with recombinant MBP-dPPR-*nad7* protein and an *nad7* specific RNA probe. The experimental setup and result presentation are similar to those in Fig. 1A. (**B**) Phenotype of *bir6-2* and dPPR-*nad7* lines. The plant phenotype of three independent dPPR-*nad7* lines was compared with WT and *bir6-2*. (**C**) Mitochondrial localization of dPPR-*nad7* fused to GFP. dPPR-*nad7*-GFP was transiently expressed in *N. benthamiana* protoplasts and cells were subsequently stained with the MitoTracker Orange CMTMRos (Invitrogen, Thermo Fisher Scientific). Fluorescence signals from GFP, the mitotracker, and chlorophyll, along with a bright-field image of the protoplast, are shown. The overlap of GFP and mitotracker fluorescence in merged image 1 demonstrates mitochondrial localization of dPPR-*nad7*-GFP, while merged image 2 excludes co-localization with chloroplasts. (**D**) Immunodetection of dPPR-*nad7* and Nad7 in mitochondrial extracts from WT, *bir6-2*, and dPPR-*nad7* lines #1–3.

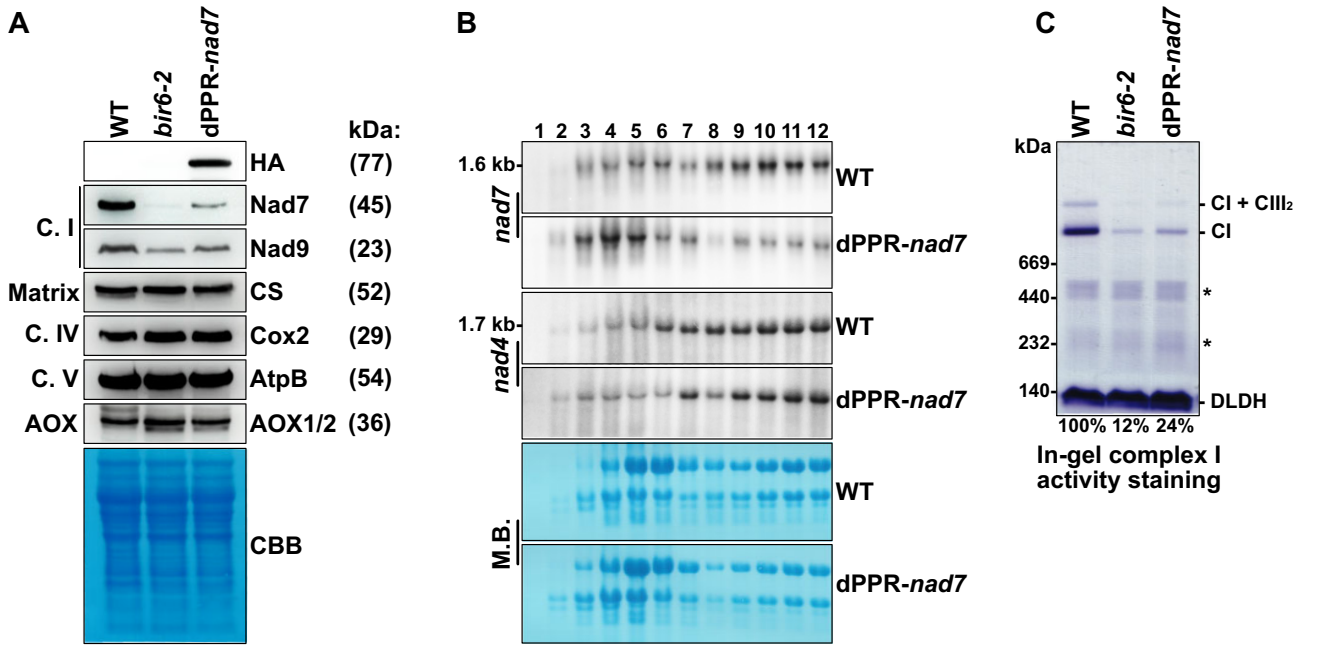


**Figure 6.** Impairment of *nad7* translation by dPPR-*nad7* expression. (**A**) Steady-state levels of Nad7 and other mitochondrial proteins were examined by immunodetection. Detected proteins are listed on the right with their molecular weights. Corresponding complexes are shown on the left. Genotypes are indicated above. CBB staining of total mitochondrial extracts was used as loading control. CS, citrate synthase. (**B**) Polysome loading analysis of *nad7* and *nad4* in WT and dPPR-*nad7* plants. The experimental setup and presentation are as described in Fig. 4B. (**C**) In-gel Complex I activity staining. Solubilized mitochondrial membrane proteins from WT, *bir6-2*, and dPPR-*nad7* plants were separated by BN–PAGE. NADH oxidase activity of Complex I was assessed by incubating the gel in an NADH/NBT mix. The sizes of the protein marker bands are indicated on the left, while the detected complexes are labeled on the right. Asterisks denote faint bands, which likely represent assembly intermediates retaining residual oxidase activity. Complex I bands were quantified using ImageJ, and the relative Complex I activity efficiency (%) compared to WT is displayed below the gel. CI, Complex I; CIII, Complex III; DLDH, dihydrolipoamide dehydrogenase.

dPPR-*nad7* suppressed *nad7* translation; however, it should be noted that although levels of Nad7 were largely decreased, the proteins were still detectable with Nad7-specific antibodies (Fig. 6A). This indicates that dPPR-*nad7* binding near the start codon interferes with translation but does not completely inhibit it. Corresponding to the decreased accumulation of Nad7 in both dPPR-*nad7* and *bir6-2*, we also observed, expectedly, reduced levels of Nad9, another component of Complex I (C. I). Proteins of other mitochondrial complexes were present at WT levels.

Polysome loading experiments revealed a shift of the peak signals of *nad7* from fractions 10, 11, and 12 in the WT to the lighter fractions 3, 4, and 5 in dPPR-*nad7* (Fig. 6B). This indicates that dPPR-nad7 binding restricts ribosome accessibility, leading to the decreased translation rates observed above. The loading with polysomes of the control transcript *nad4* in dPPR-*nad7* was comparable to that in the WT, demonstrating the specific targeting of *nad7* translation.

Complex I, also known as NADH dehydrogenase, catalyses the transfer of electrons from NADH to ubiquinone, the initial step of electron transfer during cellular respiration. It has been reported that Nad7 is essential for proper Complex I activity, and reduced levels of Nad7 impair this activity [20, 41, 42]. As demonstrated by BN–PAGE with solubilized mitochondrial membrane complexes and subsequent in-gel NADH oxidase activity staining, NADH oxidase activity of Complex I was significantly reduced in both *bir6-2* and dPPR-*nad7* mutants (Fig. 6C). This reduction in NADH oxidase activity correlates with the observed growth retardation in both mutants.

## Proteomic analysis confirms the specificity and efficiency of dPPR proteins

To comprehensively assess potential off-target effects, we conducted a quantitative proteome analysis of dPPR-*psbK* and dPPR-*nad7* plants compared to WT. Since dPPR-*psbK* and dPPR-*nad7* act on chloroplast and mitochondrial mRNAs, respectively, any off-target effects would likely involve organelle-encoded RNA and their corresponding protein products.

Using DIA, we quantified a total of 7098 proteins (Supplementary Table S2). In dPPR-*psbK* plants, 60 chloroplast-encoded proteins were identified. Consistent with our immunoblot analysis (Fig. 4A), all detected chloroplast-encoded proteins exhibited expression levels comparable to WT (fold change $< |1|$), providing no indication of physiologically relevant off-target effects (Fig. 7A). While most chloroplast-encoded proteins showed a slight downward trend in abundance, this is likely a secondary consequence of impaired PSII rather than off-target activity. Notably, the PsbK protein was not detected even in WT, likely due to its small size and the absence of suitable tryptic peptides for mass spectrometric analysis.

For dPPR-*nad7*, 20 mitochondria-encoded proteins were detected, exhibiting expression trends consistent with our immunodetection analysis (Fig. 6A): only NAD7 and NAD9 levels were markedly reduced (fold change $> |1|$), whereas all other detected mitochondria-encoded proteins displayed expression levels similar to WT (fold change $< |1|$) (Fig. 7B). These findings further support the absence of physiologically relevant off-targets.

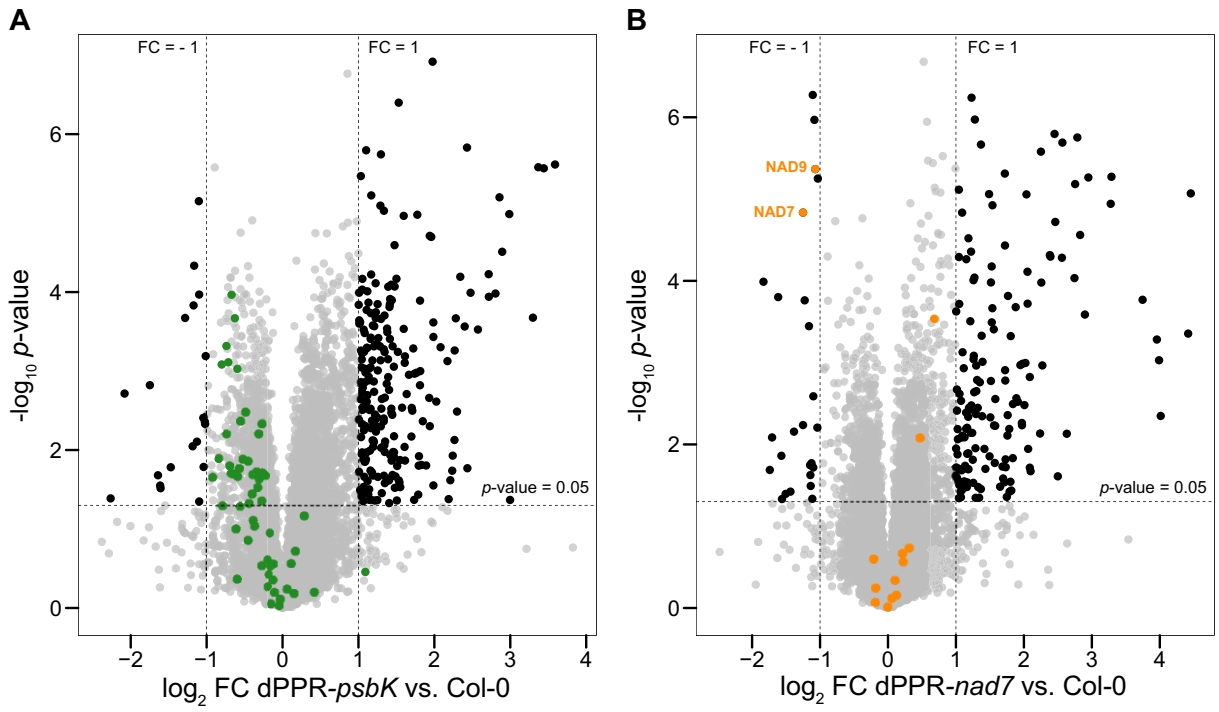


**Figure 7.** Quantitative proteomics analysis of dPPR-*psbK* and dPPR-*nad7* plants. Volcano plots displaying differentially expressed proteins (DEPs) in dPPR-*psbK* (**A**) and dPPR-*nad7* (**B**) compared to Col-0. DEPs were identified using a Student's *t*-test, with the $\log_2$ fold change plotted against the $-\log_{10}$ adjusted *P*-value. Significantly up- or downregulated nonorganellar-encoded proteins (fold change > |1|, *P*-value ≤ 0.05) are shown in black. In plot (**A**), chloroplast-encoded proteins in dPPR-*psbK* versus Col-0 are highlighted in a distinct color, while in plot (**B**) mitochondria-encoded proteins in dPPR-*nad7* versus Col-0 are marked with another distinct color. FC, fold change.

Several nonorganellar-encoded proteins showed significant up- or downregulation (fold change > |1|, *P*-value ≤ 0.05), likely reflecting secondary effects of impaired chloroplast function due to compromised PSII activity in dPPR-*psbK* or disrupted mitochondrial electron transport in dPPR-*nad7* plants (black dots in Fig. 7). Indeed, gene ontology enrichment analysis revealed that most downregulated proteins were associated with photosynthetic processes in dPPR-*psbK* or mitochondrial oxidative phosphorylation in dPPR-*nad7* (Supplementary Fig. S7). Among the up-regulated proteins in both dPPR-*psbK* and dPPR-*nad7*, the majority were associated with organellar RNA metabolism. Since dPPR proteins influence specific organellar mRNAs, their perturbation may trigger a cellular stress response, leading to increased expression of factors involved in RNA stability, splicing, or processing to maintain organellar gene expression and function. This could be part of a broader retrograde signaling mechanism, in which organellar dysfunction induces nuclear-encoded gene expression changes to restore homeostasis.

In conclusion, the engineered dPPR proteins exhibited correct targeting and effectively inhibited the translation of specific organellar transcripts, as shown by the successful translation suppression of *psbK* in chloroplasts and *nad7* in mitochondria, with no obvious off-target effects. These findings highlight the potential of dPPRs as versatile tools for manipulating gene expression in organelles, offering new avenues for functional studies and genetic engineering.

## Discussion

The application of synthetic dPPR proteins to target and inhibit the translation of specific organellar mRNAs represents a significant advancement in plant molecular biology. Our study demonstrates the efficiency of two dPPR proteins, dPPR-*psbK* and dPPR-*nad7*, in selectively reducing the translation rates of *psbK* and *nad7* mRNAs, respectively. These findings have broad implications for the study and manipulation of organellar gene expression, with potential applications across all eukaryotes amenable to nuclear transformation.

The resulting *psbK* phenotype in Arabidopsis dPPR-*psbK* plants, characterized by reduced PSII efficiency and impaired supercomplex formation, underscores the critical role of PsbK in PSII formation. These observations support previous suggestions, based on the structure of PSII, that PsbK could play a role in the integration of LHCII into PSII supercomplexes [43–45]. The reduction in PSII supercomplex levels and the accumulation of free LHCII trimers in transgenic dPPR-*psbK* Arabidopsis and tobacco *psbK* knockout lines provide strong evidence of PsbK's role in the formation of PSII supercomplexes.

In contrast, effects of reduced levels of Nad7 on mitochondrial respiration has already been documented in earlier studies [20, 46, 47]. Our use of dPPR-*nad7* to target the *nad7* mRNA downstream of its start codon aimed to partially inhibit its translation, thereby avoiding potential lethality associated with complete knockout. However, some primary transformants expressing a GFP fusion of dPPR-*nad7* (dPPR-*nad7*-GFP) exhibited even more pronounced growth retardation and were either sterile or not capable of producing sufficient viable seeds for further work (Supplementary Fig. S8). Although dPPR-*nad7*-GFP targets the same *nad7* sequence as dPPR-*nad7*, the bulky GFP tag seems to enhance the restriction of ribosome accessibility and consequently worsen the phenotype of transgenic plants. In future studies, the use of

inducible promoter systems could provide a valuable solution to prevent lethality. Such systems would allow for temporal control over dPPR expression, enabling the study of gene function at specific developmental stages or in response to particular environmental conditions, while avoiding the severe developmental defects associated with constitutive knockdown. In our study, the phenotypic similarities between our viable dPPR-*nad7* lines and the *bir6-2* mutant further validate our approach and highlight the utility of dPPRs in studying mitochondrial gene function.

Designer PPR proteins have demonstrated high specificity for their intended RNA targets, although some degree of off-target binding has been noted. Importantly, these off-target interactions generally lacked physiological significance. For instance, McDermott *et al.* [16] reported minimal off-target binding by a synthetic PPR protein designed for the 3′ UTR of *psaA* mRNA in chloroplasts reveled by RIP-Seq analysis. Similarly, Manavski *et al.* [18] and Rojas *et al.* [19] documented some off-target binding using analogous synthetic PPR designs. Manavski *et al.* [18] observed that while designer PPR proteins could stabilize the endogenous chloroplast *rbcL* mRNA, a few off-target interactions were detected. Likewise, Rojas *et al.* [19] noted a fair number of off-target interactions when employing synthetic PPR proteins to investigate *psbA* translation control in Arabidopsis chloroplasts. However, across these studies, the physiological impact of off-target binding, predominantly involving RNAs with sequence similarity to the intended targets, was found to be minimal. Our RIP-slot blot analysis and phenotypic comparisons with the reference mutants also largely exclude any physiologically relevant off-targets. The phenotypic similarities between our dPPR-*psbK* and dPPR-*nad7* lines and the respective reference mutants (*psbK* knockouts in tobacco and *bir6-2* mutants) strongly suggest that any potential off-targets did not have significant physiological impacts.

In the future, studies could be conducted to increase the specificity of dPPR proteins and reduce potential off-target effects. For example, refining the PPR code and incorporating additional specificity-determining residues beyond the canonical 5th and 35th amino acids could enhance target recognition precision. Also implementing machine learning algorithms to predict and optimize PPR–RNA interactions could lead to more accurate designs that minimize off-target binding while maintaining high on-target affinity.

In conclusion, our study demonstrates the power of engineered PPR proteins as tools for targeted translation inhibition, providing a means to investigate chloroplast and mitochondrial gene function in plants beyond just tobacco. While challenges remain, particularly regarding the specificity of binding and the potential lethality of strong knockdown lines, this approach offers unprecedented precision in manipulating organellar gene expression. As we continue to refine these techniques, we anticipate that engineered dPPR proteins will become increasingly valuable tools for unraveling the complexities of organellar gene regulation and function in plants. This technique is particularly advantageous in mitochondria for adjusting transcript quantities and exploring the mechanisms controlling the expression and assembly of multisubunit mitochondrial complexes. These processes remain poorly studied due to the lack of suitable methods for manipulating gene expression in mitochondria and also due to the embryo lethality of mutations in components of respiratory complexes [48]. dPPR proteins inhibiting specifically the translation of mitochondrial subunits under the control of inducible promoters could overcome these limitations, paving the way for more comprehensive studies of mitochondrial gene function.

## Acknowledgements

We thank Stefanie Volz for her assistance in generating the tobacco psbK knockout construct. We are also grateful to Etienne Meyer and Kristina Kühn (University of Halle) for providing the *bir6-2* T-DNA line and for helpful discussions, and Alice Barkan (University of Oregon) for supplying the pMAL-Tev vector. Additionally, we thank the core facility MS-BioLMU for mass spectrometry analysis.

*Author contributions*: N.M. conceived and designed research. N.M., S.S., and J.M. performed the experiments. N.M., S.S., H.-H.K., D.L., and J.M. analyzed the data. N.M. wrote the manuscript with contributions from all co-authors.

## Supplementary data

Supplementary data is available at NAR online.

## Conflict of interest

None declared.

## Funding

This research was supported by the German Research Foundation [TR175 B07] to D.L., [TR175 A03] to J.M., [TR175 B06] to S.S., and [TR175 B09] to H.-H.K. Funding to pay the Open Access publication charges for this article was provided by the Deutsche Forschungsgemeinschaft [TR175 B09].

## Data availability

The mass spectrometry proteomics data have been deposited to the ProteomeXchange Consortium via the PRIDE partner repository with the dataset identifier PXD060146. All raw data underlying this article will be shared on reasonable request to the corresponding author.

## References

1. Martin W, Rujan T, Richly E *et al.* Evolutionary analysis of arabidopsis, cyanobacterial, and chloroplast genomes reveals plastid phylogeny and thousands of cyanobacterial genes in the nucleus. *Proc Natl Acad Sci USA* 2002;**99**:12246–51. https://doi.org/10.1073/pnas.182432999
2. Marienfeld J, Unseld M, Brennicke A. The mitochondrial genome of Arabidopsis is composed of both native and immigrant information. *Trends Plant Sci* 1999;**4**:495–502. https://doi.org/10.1016/S1360-1385(99)01502-2
3. Svab Z, Hajdukiewicz P, Maliga P. Stable transformation of plastids in higher plants. *Proc Natl Acad Sci USA* 1990;**87**:8526–30. https://doi.org/10.1073/pnas.87.21.8526
4. Kazama T, Okuno M, Watari Y *et al.* Curing cytoplasmic male sterility via TALEN-mediated mitochondrial genome editing. *Nat Plants* 2019;**5**:722–30. https://doi.org/10.1038/s41477-019-0459-z
5. Forner J, Kleinschmidt D, Meyer EH *et al.* Targeted introduction of heritable point mutations into the plant mitochondrial genome. *Nat Plants* 2022;**8**:245–56. https://doi.org/10.1038/s41477-022-01108-y

6. Forner J, Kleinschmidt D, Meyer EH *et al.* Targeted knockout of a conserved plant mitochondrial gene by genome editing. *Nat Plants* 2023;**9**:1818–31. https://doi.org/10.1038/s41477-023-01538-2
7. Kang BC, Bae SJ, Lee S *et al.* Chloroplast and mitochondrial DNA editing in plants. *Nat Plants* 2021;**7**:899–905. https://doi.org/10.1038/s41477-021-00943-9
8. Val R, Wyszko E, Valentin C *et al.* Organelle trafficking of chimeric ribozymes and genetic manipulation of mitochondria. *Nucleic Acids Res* 2011;**39**:9262–74. https://doi.org/10.1093/nar/gkr580
9. Niazi AK, Delannoy E, Khalid Iqbal R *et al.* Mitochondrial transcriptome control and intercompartment cross-talk during plant development. *Cells* 2019;**8**:583. https://doi.org/10.3390/cells8060583
10. Colas des Francs-Small C, Vincis Pereira Sanglard L, Small I. Targeted cleavage of nad6 mRNA induced by a modified pentatricopeptide repeat protein in plant mitochondria. *Commun Biol* 2018;**1**:166. https://doi.org/10.1038/s42003-018-0166-8
11. Vincis Pereira Sanglard L, Small ID, Colas des Francs-Small C. Alteration of mitochondrial transcript expression in Arabidopsis thaliana using a custom-made library of pentatricopeptide repeat proteins. *Int J Mol Sci* 2023;**24**:13233. https://doi.org/10.3390/ijms241713233
12. Yang F, Pereira Sanglard LV, Lee CP *et al.* Mitochondrial atp1 mRNA knockdown by a custom-designed pentatricopeptide repeat protein alters ATP synthase. *Plant Physiol* 2024;**194**:2631–47. https://doi.org/10.1093/plphys/kiae008
13. Kwok Van Der Giezen F, Honkanen S, Colas Des Francs-Small C *et al.* Applications of synthetic pentatricopeptide repeat proteins. *Plant Cell Physiol* 2024;**65**:503–15. https://doi.org/10.1093/pcp/pcad150
14. Barkan A, Small I. Pentatricopeptide repeat proteins in plants. *Annu Rev Plant Biol* 2014;**65**:415–42. https://doi.org/10.1146/annurev-arplant-050213-040159
15. Shen C, Wang X, Liu Y *et al.* Specific RNA recognition by designer pentatricopeptide repeat protein. *Mol Plant* 2015;**8**:667–70. https://doi.org/10.1016/j.molp.2015.01.001
16. McDermott JJ, Watkins KP, Williams-Carrier R *et al.* Ribonucleoprotein capture by *in vivo* expression of a designer pentatricopeptide repeat protein in Arabidopsis. *Plant Cell* 2019;**31**:1723–33. https://doi.org/10.1105/tpc.19.00177
17. Manavski N, Abdel-Salam E, Schwenkert S *et al.* Targeted introduction of premature stop codon in plant mitochondrial mRNA by a designer pentatricopeptide repeat protein with C-to-U editing function. *Plant J* 2025;**121**:e17247. https://doi.org/10.1111/tpj.17247
18. Manavski N, Mathieu S, Rojas M *et al.* In vivo stabilization of endogenous chloroplast RNAs by customized artificial pentatricopeptide repeat proteins. *Nucleic Acids Res* 2021;**49**:5985–97. https://doi.org/10.1093/nar/gkab390
19. Rojas M, Chotewutmontri P, Barkan A. Translational activation by a synthetic PPR protein elucidates control of psbA translation in Arabidopsis chloroplasts. *Plant Cell* 2024;**36**:4168–78. https://doi.org/10.1093/PLCELL/KOAE112
20. Koprivova A, Francs-Small CCD, Calder G *et al.* Identification of a pentatricopeptide repeat protein implicated in splicing of intron 1 of mitochondrial nad7 transcripts. *J Biol Chem* 2010;**285**:32192–9. https://doi.org/10.1074/jbc.M110.147603
21. Sweetlove LJ, Taylor NL, Leaver CJ. Isolation of intact, functional mitochondria from the model plant *Arabidopsis thaliana*. *Methods Mol Biol* 2007;**372**:125–36. https://doi.org/10.1007/978-1-59745-365-3_9
22. Lyska D, Engelmann K, Meierhoff K *et al.* pAUL: a gateway-based vector system for adaptive expression and flexible tagging of proteins in Arabidopsis. *PLoS One* 2013;**8**:e53787. https://doi.org/10.1371/journal.pone.0053787
23. Sugiura M, Shinozaki K, Zaita N *et al.* Clone bank of the tobacco (*Nicotiana tabacum*) chloroplast genome as a set of overlapping restriction endonuclease fragments: mapping of eleven ribosomal protein genes. *Plant Sci* 1986;**44**:211–7. https://doi.org/10.1016/0168-9452(86)90093-2
24. Svab Z, Maliga P. High-frequency plastid transformation in tobacco by selection for a chimeric aadA gene. *Proc Natl Acad Sci USA* 1993;**90**:913–7. https://doi.org/10.1073/pnas.90.3.913
25. Schwenkert S, Umate P, Dal Bosco C *et al.* PsbI affects the stability, function, and phosphorylation patterns of photosystem II assemblies in tobacco. *J Biol Chem* 2006;**281**:34227–38. https://doi.org/10.1074/jbc.M604888200
26. Vincis Pereira Sanglard L, Colas des Francs-Small C. High-throughput BN–PAGE for mitochondrial respiratory complexes. *Methods Mol. Biol.* 2022;**2363**:111–9. https://doi.org/10.1007/978-1-0716-1653-6_10
27. Umate P, Fellerer C, Schwenkert S *et al.* Impact of PsbTc on forward and back electron flow, assembly, and phosphorylation patterns of photosystem II in tobacco. *Plant Physiol* 2008;**148**:1342–53. https://doi.org/10.1104/pp.108.126060
28. Barkan A. Nuclear mutants of maize with defects in chloroplast polysome assembly have altered chloroplast RNA metabolism. *Plant Cell* 1993;**5**:389–402. https://doi.org/10.2307/3869720
29. Marino G, Naranjo B, Wang J *et al.* Relationship of GUN1 to FUG1 in chloroplast protein homeostasis. *Plant J* 2019;**99**:521–35. https://doi.org/10.1111/tpj.14342
30. Rappsilber J, Ishihama Y, Mann M. Stop and go extraction tips for matrix-assisted laser desorption/ionization, nanoelectrospray, and LC/MS sample pretreatment in proteomics. *Anal Chem* 2003;**75**:663–70. https://doi.org/10.1021/ac026117i
31. Demichev V, Messner CB, Vernardis SI *et al.* DIA-NN: neural networks and interference correction enable deep proteome coverage in high throughput. *Nat Methods* 2020;**17**:41–4. https://doi.org/10.1038/s41592-019-0638-x
32. Gerault MA, Camoin L, Granjeaud S. DIAgui: a Shiny application to process the output from DIA-NN. *Bioinform Adv* 2024;**4**:vbae001. https://doi.org/10.1093/bioadv/vbae001
33. Cox J, Hein MY, Luber CA *et al.* Accurate proteome-wide label-free quantification by delayed normalization and maximal peptide ratio extraction, termed MaxLFQ. *Mol Cell Proteomics* 2014;**13**:2513–26. https://doi.org/10.1074/mcp.M113.031591
34. Tyanova S, Temu T, Cox J. The MaxQuant computational platform for mass spectrometry-based shotgun proteomics. *Nat Protoc* 2016;**11**:2301–19. https://doi.org/10.1038/nprot.2016.136
35. R Core Team. *R A Language and Environment for Statistical Computing*. R Foundation for Statistical Computing, Vienna. Scientific Research Publishing, 2022.
36. Posit Team. *RStudio Integrated Development Environment for R*. Posit Software, PBC, Boston, MA: Scientific Research Publishing, 2024.
37. Han LJ, Fan DY, Wang XP *et al.* The protective role of non-photochemical quenching in PSII photo-susceptibility: a case study in the field. *Plant Cell Physiol* 2023;**64**:43–54. https://doi.org/10.1093/pcp/pcac137
38. Takahashi Y, Matsumoto H, Goldschmidt-Clermont M *et al.* Directed disruption of the Chlamydomonas chloroplast psbK gene destabilizes the photosystem II reaction center complex. *Plant Mol Biol* 1994;**24**:779–88. https://doi.org/10.1007/BF00029859
39. Zhang ZH, Mayes SR, Vass I *et al.* Characterization of the psbK locus of synechocystis sp. PCC 6803 in terms of photosystem II function. *Photosynth Res* 1993;**38**:369–77. https://doi.org/10.1007/BF00046763
40. Iwai M, Suzuki T, Kamiyama A *et al.* The PsbK subunit is required for the stable assembly and stability of other small subunits in the PSII complex in the thermophilic cyanobacterium thermosynechococcus elongatus BP-1. *Plant Cell Physiol* 2010;**51**:554–60. https://doi.org/10.1093/pcp/pcq020
41. Hammani K, Des Francs-Small CC, Takenaka M *et al.* The pentatricopeptide repeat protein OTP87 is essential for RNA editing of nad7 and atp1 transcripts in Arabidopsis mitochondria. *J Biol Chem* 2011;**286**:21361–71. https://doi.org/10.1074/jbc.M111.230516

42. Pineau B, Mathieu C, Gérard-Hirne C *et al.* Targeting the NAD7 subunit to mitochondria restores a functional complex I and a wild type phenotype in the Nicotiana sylvestris CMS II mutant lacking nad7. *J Biol Chem* 2005;**280**:25994–6001. https://doi.org/10.1074/jbc.M500508200
43. Sheng X, Liu X, Cao P *et al.* Structural roles of lipid molecules in the assembly of plant PSII–LHCII supercomplex. *Biophys Rep* 2018;**4**:189–203. https://doi.org/10.1007/s41048-018-0068-9
44. Albanese P, Tamara S, Saracco G *et al.* How paired PSII–LHCII supercomplexes mediate the stacking of plant thylakoid membranes unveiled by structural mass-spectrometry. *Nat Commun* 2020;**11**:1361. https://doi.org/10.1038/s41467-020-15184-1
45. Shen L, Huang Z, Chang S *et al.* Structure of a C2S2M2N2-type PSII–LHCII supercomplex from the green alga *Chlamydomonas reinhardtii*. *Proc Natl Acad Sci USA* 2019;**116**:21246–55. https://doi.org/10.1073/pnas.1912462116
46. Hsieh WY, Liao JC, Chang CY *et al.* The SLOW GROWTH3 pentatricopeptide repeat protein is required for the splicing of mitochondrial NADH dehydrogenase Subunit7 intron 2 in Arabidopsis. *Plant Physiol* 2015;**168**:490–501. https://doi.org/10.1104/pp.15.00354
47. Ayabe H, Toyoda A, Iwamoto A *et al.* Mitochondrial gene defects in Arabidopsis can broadly affect mitochondrial gene expression through copy number. *Plant Physiol* 2023;**191**:2256–75. https://doi.org/10.1093/plphys/kiad024
48. Mansilla N, Racca S, Gras DE *et al.* The complexity of mitochondrial Complex IV: an update of cytochrome c oxidase biogenesis in plants. *Int J Mol Sci* 2018;**19**:662. https://doi.org/10.3390/ijms19030662

**Received:** October 19, 2024. **Revised:** March 3, 2025. **Editorial Decision:** March 4, 2025. **Accepted:** March 11, 2025